

Electrochemically Driven Giant Resistive Switching in Perovskite Nickelates Heterostructures

Le Wang, Qinghua Zhang, Lei Chang, Lu You, Xu He, Kuijuan Jin, Lin Gu, Haizhong Guo, Chen Ge, Yaqing Feng, and Junling Wang*

The rich phase diagrams and peculiar physical properties of rare earth perovskite nickelates (RNiO₃) have recently attracted much attention. Their electronic structures are highly sensitive to carrier density and bandwidth due to Mott physics. Here, the electrochemically driven giant resistive switching in Pt/RNiO₃/Nb-SrTiO₃ heterostructures is reported. Systematic investigation confirms that oxygen vacancies migration modifies the interfacial barrier at the RNiO₃/Nb-SrTiO₃ interface and causes the resistive switching behavior. An ON/OFF ratio of about 10⁵ at room temperature is observed, which can be modulated by controlling the oxygen vacancies during sample fabrication or by varying the rare earth element in RNiO₃. The findings provide an important step forward toward the development of multifunctional electronic devices based on perovskite nickelates.

Perovskite rare earth nickelates (RNiO₃) sit right at the boundary between charge-transfer and Mott insulators, attracting much interest recently. Researchers can tune certain parameters, such as the on-site Coulomb repulsion energy U , charge transfer energy Δ , or bandwidth W , to investigate the transition between these two types of insulators and engineer exotic phenomena.^[1–7] It is known that the properties of RNiO₃ depend on the rare earth element. A smaller R decreases the tolerance factor and subsequently the Ni–O–Ni bond angle, leading to a reduction of W , which drives the system deeper into the insulating state.^[8]

Another unique property of RNiO₃ that is usually overlooked is the weak Ni–O bond and small oxygen vacancy formation energy,^[9] making them very susceptible to the formation and migration of oxygen vacancies. Introducing oxygen vacancies


into the corner-shared NiO₆ octahedra network (Figure 1a) modifies the Ni–O bond length and angle, affecting the electronic bandwidth and physical properties of RNiO₃. Furthermore, Ni³⁺ is reduced to Ni²⁺ ($2\text{Ni}^{3+} + \text{O}_\text{o}^\times \leftrightarrow 2\text{Ni}^{2+} + \text{V}_\text{o}^{2+} + \frac{1}{2}\text{O}_2$) and electrons are doped into RNiO₃ via oxygen vacancies.^[2,10] Previous works have shown that oxygen vacancies play an important role in perovskite heterostructures.^[10–15] External electric field could induce the migration of the oxygen vacancy in the perovskite films and then change the interfacial barrier in heterostructures, leading resistive switching (RS) behavior. We expect such effect to be more

prominent in nickelates-based ones due to their smaller oxygen vacancy formation energy. This motivates us to explore the possibility of electrochemically driven RS in nickelates systems. Our finding reveals giant bipolar RS behavior in Pt/RNiO₃/Nb-SrTiO₃ heterostructures with ON/OFF ratio of about 10⁵ at room temperature. The effect is tunable by varying the oxygen content or changing the rare earth element in the sample.

A set of GdNiO_{3–x} films on Nb-SrTiO₃ substrates were grown under different deposition oxygen pressures ($P(\text{O}_2)$) of 100, 20, 2, and 0.2 mTorr, respectively. The film thickness was fixed at 10 nm. The samples are labeled as D1–D4, in the order of decreasing $P(\text{O}_2)$ from 100 to 0.2 mTorr. The influence of $P(\text{O}_2)$ on our samples can be seen in Figure 1 (also see Figure S1 in the Supporting Information). Figure 1b displays the typical current–voltage (I – V) characteristics of the samples, and the inset is the schematic setup for the measurements. The arrows in Figure 1b represent the sequence of voltage sweeps. Sample D1 shows nonlinear I – V characteristics with negligible RS effect. In contrast, sample D4 shows obvious “counterclockwise” bipolar RS behavior. Here, we define the upper and lower branches of the I – V curves as low resistance state (LRS or ON) and high resistance state (HRS or OFF), respectively. Sample D4 switches from HRS (LRS) to LRS (HRS) when a forward (reverse) bias is applied to Pt, and this is defined as the set (reset) process. It should be pointed out that this counterclockwise I – V hysteresis in our asymmetrical devices is different from ferroelectric switchable diode behavior,^[16–18] which is mainly controlled by the ferroelectric polarization. Since the formation energy of oxygen vacancy is low in nickelates,^[9] we expect more oxygen vacancies in the GdNiO_{3–x} film than in the Nb-SrTiO₃ substrate. Scanning transmission electron

Dr. L. Wang, L. Chang, Dr. L. You, Prof. J. Wang
School of Materials Science and Engineering
Nanyang Technological University
Singapore 639798, Singapore
E-mail: jlwang@ntu.edu.sg

Dr. Q. Zhang, Dr. X. He, Prof. K. Jin, Prof. L. Gu, Dr. H. Guo,
Dr. C. Ge, Y. Feng
Institute of Physics
Chinese Academy of Sciences
Beijing 100190, China
Prof. K. Jin, Prof. L. Gu
Collaborative Innovation Center of Quantum Matter
Beijing 100190, China

 The ORCID identification number(s) for the author(s) of this article can be found under <https://doi.org/10.1002/aelm.201700321>.

DOI: 10.1002/aelm.201700321

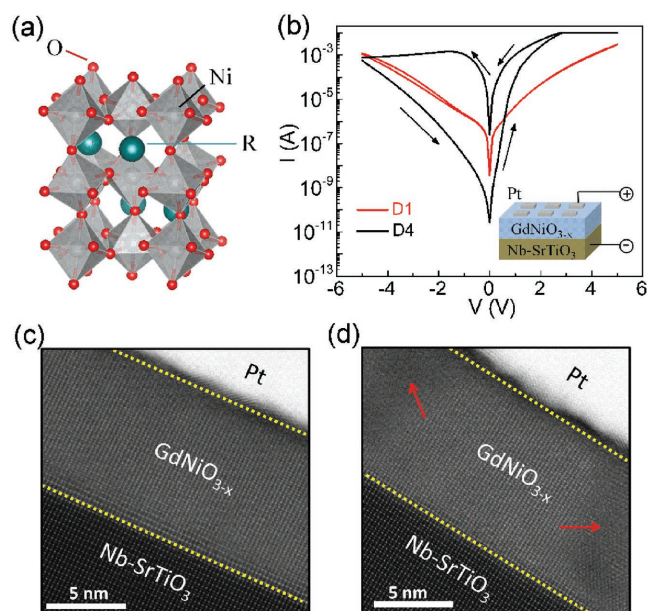


Figure 1. *I*–*V* characteristics of the devices. a) The distorted perovskite structure of the RNiO₃ crystal. b) *I*–*V* curves of samples D1 and D4 plotted on semilogarithmic scale. The direction of bias sweeping is indicated by arrows. The inset shows the schematic of the testing device. c) HAADF image of sample D1. d) HAADF image of sample D4. Red arrows in panel (d) show poor crystallinity induced by local oxygen vacancies.

microscope (STEM) results confirm that the concentration of oxygen vacancies is higher in GdNiO_{3-x} films deposited under lower P(O₂). High-angle annular dark-field (HAADF) images of samples D1 and D4 along the [110] projection are shown in Figure 1c,d, where the image contrast is approximately proportional to Z² (Z is the atomic number of element). The good epitaxial relationship between GdNiO_{3-x} and Nb-SrTiO₃ can be observed in both films. The uniform atomic columns in Figure 1c demonstrate the high crystallinity of sample D1. In comparison, clear contrast as indicated by two red arrows in Figure 1d suggests poor crystallinity of sample D4 induced by local oxygen vacancies. Oxygen vacancy induced dark contrast can also be found in the low-magnification image (see Figure S2 in the Supporting Information). The fact that low P(O₂) leads to more oxygen vacancies has also been reported for other oxide materials.^[13,19–22] Figure 1b and Figure S3 (Supporting Information) clearly show more pronounced *I*–*V* hysteresis for GdNiO_{3-x} films grown under lower P(O₂), suggesting that oxygen vacancies in GdNiO_{3-x} films play a crucial role in the RS behavior. Our subsequent analysis thus focuses on sample D4.

Based on the *I*–*V* curves, a large ON/OFF ratio of about 10⁵ in resistance change is achieved, as shown in Figure 2a. Accompanying the resistance change, a forward scan to +5 V also switches the device to a high capacitance state (HCS), while a reverse scan to –5 V drives the device to a low capacitance state (LCS). The concurrent resistance and capacitance switching behaviors suggest that bias modified interfacial barrier is likely the origin.^[12,14] Unlike unipolar RS memories, this bipolar RS does not require an initial forming step and show continuously tunable resistance, which are advantages for practical

applications.^[23,24] For nonvolatile memories, large ON/OFF ratio, high writing speed, long data retention, and good fatigue property are important. We have measured about 60 randomly selected Pt/GdNiO_{3-x}(0.2 mTorr)/Nb-SrTiO₃ devices. As shown in Figure 2b, the ON/OFF ratios fall in the range of 10⁴–10⁵, showing good reproducibility and uniformity.

To investigate the operation speed of the RS-based nonvolatile memory, we have measured the influence of pulse width on the switching from HRS (LRS) to LRS (HRS). Before the measurements, the device was first set to HRS (LRS) by applying a voltage pulse of –5 V (+5 V) with duration of 1 s. Then, square pulses (±5 V) from 1 μs to 1 s were applied, and the resistance of the device was subsequently recorded at a bias of –0.2 V. As shown in Figure 2c,d, the transition from LRS to HRS is slower than from HRS to LRS, while both cases can be completed using 100 μs pulses. Note that the switching time can be reduced to around 1 μs by using higher voltage.

Figure 2e shows the retention characteristic of the device at a reading bias of –0.2 V. An ON/OFF ratio of over three orders of magnitude can still be retained after ten years by extrapolating the retention data. The fatigue performance was tested by switching the device repeatedly using +5 and –5 V pulses of 150 μs. The write (from HRS to LRS) and erase (from LRS to HRS) operations exhibit good endurance. As shown in Figure 2f, no significant change in the ON/OFF is observed after more than 10⁴ write/read cycles.

To elucidate the RS mechanism, it is first necessary to clarify the major contribution to the observed resistance. The work function of Pt is ≈5.3 eV, while the work function of GdNiO_{3-x} is ≈4.3 eV (Figure 3). Since perovskite nickelates usually behave like p-type semiconductors,^[25,26] an Ohmic contact at the Pt/GdNiO_{3-x} interface is expected and indeed observed (see Figure S4 in the Supporting Information). Furthermore, the *I*–*V* curves for a Pt/GdNiO_{3-x}/SrRuO₃ heterostructure show negligible RS effect (see Figure S4 in the Supporting Information), even though the GdNiO_{3-x} films were grown under the same P(O₂) of 0.2 mTorr. Therefore, we can conclude that it is not the bulk of GdNiO_{3-x} but the GdNiO_{3-x}/Nb-SrTiO₃ interface that plays an important role in the observed RS. As an n-type semiconductor, E_F of Nb-SrTiO₃ is close to the bottom of the conduction band and the difference is merely 0.01 eV.^[27] Thus, the GdNiO_{3-x}/Nb-SrTiO₃ interface can be treated as a p–n heterojunction. Noted that the RS behavior in our device comes from this p–n heterojunction, not from the metal/Nb-SrTiO₃ Schottky barrier.^[28,29] To study the switching behavior of this p–n heterojunction, the conduction property during the whole RS should be investigated.

Figure 3a shows the *I*–*V* curves of sample D4 on a linear scale. Clear RS is observed with the forward (reverse) bias leading to LRS (HRS). During the measurement, the current undergoes a gradual change, suggesting that the RS process is not related to filaments (also see Figure S5 in the Supporting Information).^[30] A compliance current of 10 mA was applied to the set operation to prevent the device from permanent breakdown. *I*–*V* curve in HRS shows good rectifying behavior. The rectification ratio at ±1.5 V is 5.5 × 10³ for HRS, and it decreases to 2 for LRS. Both LRS and HRS show nonlinear *I*–*V* curves. Three main conduction mechanisms, including space charge limited conduction (SCLC), Schottky emission, and

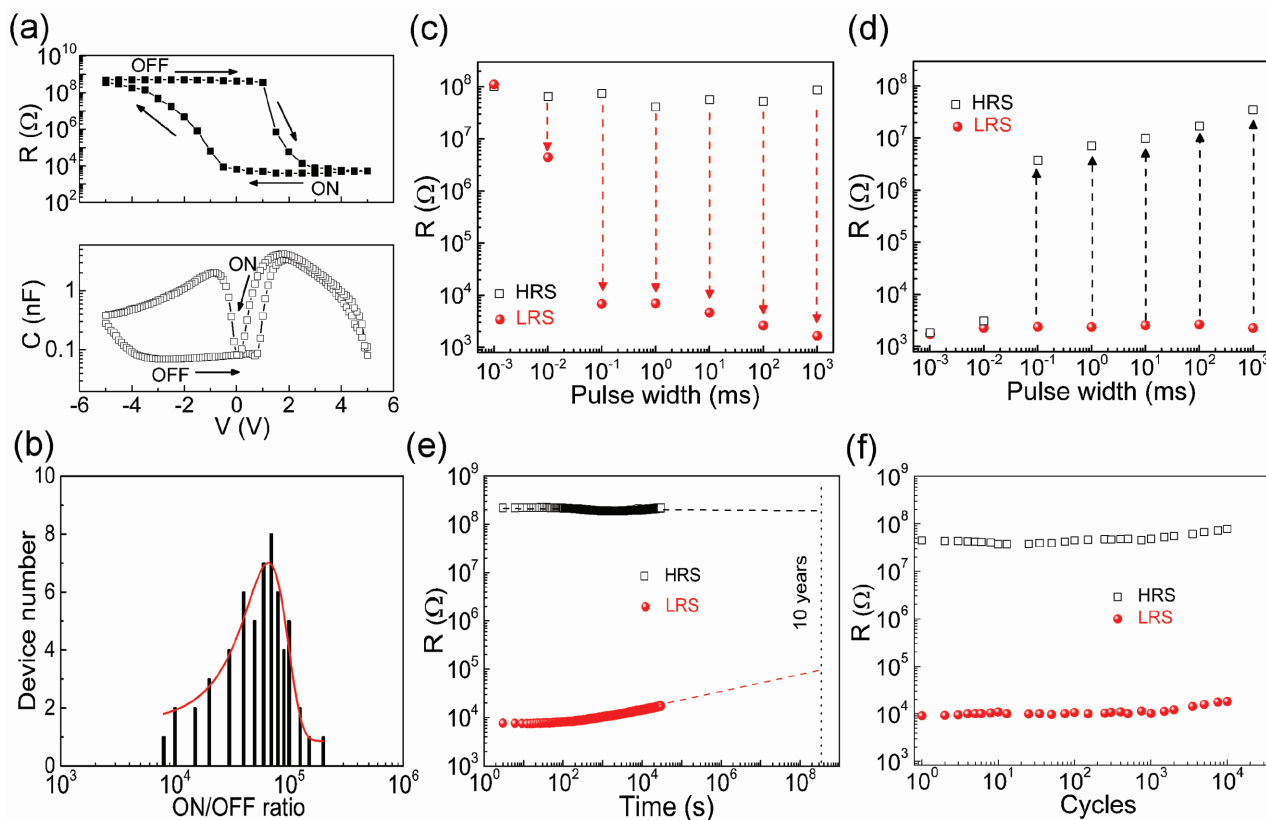


Figure 2. Device performance. a) Resistance (R) and capacitance (C) of sample D4 as functions of applied voltage. The C - V curve is extracted from impedance measurements with a 10 mV, 25 kHz AC signal imposed on a continuous DC bias sweep. b) ON/OFF ratios measured on about 60 devices. R evolution of the device after c) writing or d) erasing with decreasing voltage pulse width from 1 s to 1 μ s. Before the writing (erasing) operations, voltage pulses of -5 V ($+5$ V) with a pulse width of 1 s are used to set the device to the HRS (LRS). e) HRS and LRS retention characteristic of the device recorded at -0.2 V after a forward and reverse bias sweep, respectively. f) Fatigue performance of the device.

Poole-Frenkel (P-F) emission were used to fit the nonlinear I - V curves.^[31,32] For SCLC, the I - V curve follow the Child's law^[33]

$$J \propto \frac{8}{9} \epsilon_r \epsilon_0 \mu \frac{E^2}{d} \quad (1)$$

where J is the current density, ϵ_r is the relative dielectric constant, ϵ_0 is the permittivity of free space, μ is the mobility of charge carriers, E is the electric field, and d is the film thickness. For Schottky emission, the I - V relationship could be expressed as following^[34]

$$I \propto T^2 \exp \left[\frac{e \sqrt{(eV)/(4\pi\epsilon_r\epsilon_0 d)}}{k_B T} \right] \quad (2)$$

where e is the electronic charge, k_B is the Boltzmann constant, T is the measured temperature. If the leakage is controlled by P-F emission, the I - V relationship is as following^[34]

$$I/V \propto \exp \left[\frac{e \sqrt{(eV)/(\pi\epsilon_r\epsilon_0)}}{rk_B T} \right] \quad (3)$$

where r is a coefficient ranging between 1 and 2, depending on the exact position of the Fermi level.^[35] I - V curves of both HRS and LRS are plotted in double-logarithmic scales in Figure 3b. The fitting results are also highlighted by color lines. The LRS follows the SCLC mechanism (slope should be around 2 according to Child's law).^[33] On the other hand, the I - V characteristics of HRS are complicated and can be divided into two regions. It is dominated by Schottky emission under low electric field and P-F emission under high electric field. These fitting results are consistent with the interfacial effect on RS,^[31,36,37] where the migration of oxygen vacancies at the interface drives RS.

Figure 3c illustrates the RS behavior at the $\text{GdNiO}_{3-x}/\text{Nb-SrTiO}_3$ interface. When a low forward bias is applied to the device, the positively charged oxygen vacancies are gradually driven from the GdNiO_{3-x} films into the Nb-SrTiO₃ substrates, thus inducing the change of oxygen vacancy concentration in GdNiO_{3-x} films. The decrease of oxygen vacancies concentration reduces both E_g and E_F of GdNiO_{3-x} films (Figure 3d; Figure S6, Supporting Information). A reduction of potential barrier for electron or hole injection and depletion region width (W_d) could be expected, which leads to LRS and HCS of the heterostructure (Figure 2a). On the other hand, when a reverse bias pushes these oxygen vacancies back to the GdNiO_{3-x} films,

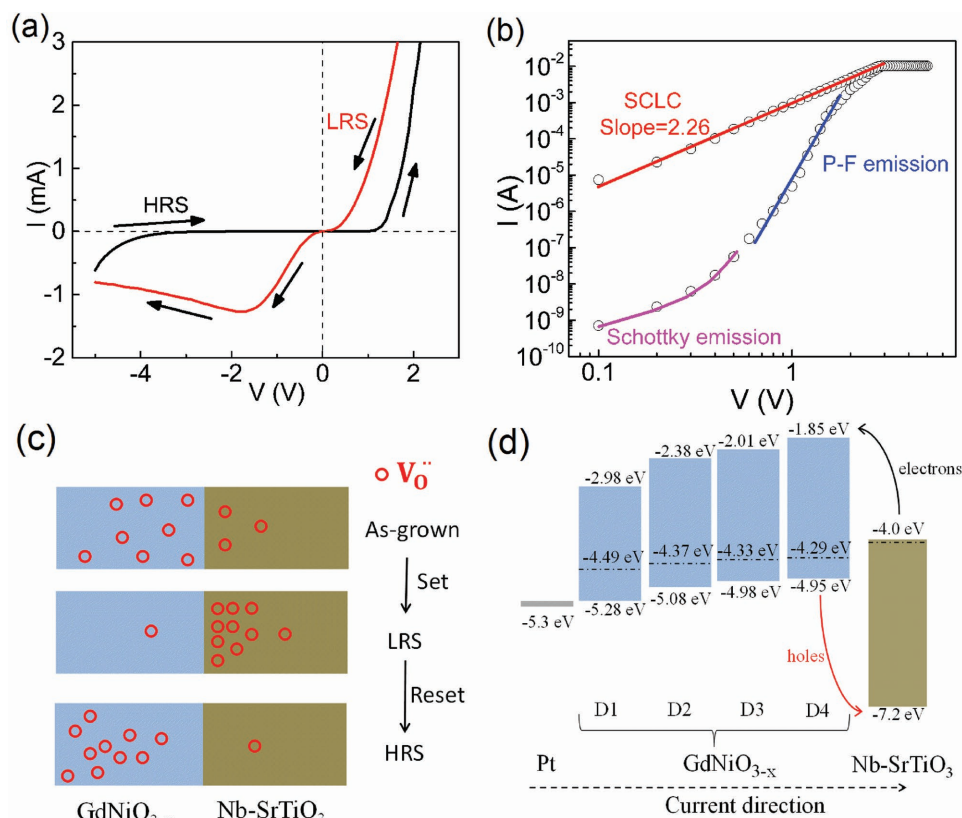


Figure 3. Resistive switching mechanism. a) Linear scale I - V switching characteristics of sample D4 as the voltage sweeps from -5 to 0 , $+5$ V, and then back to -5 V. b) Fittings for the nonlinear I - V curves of the GdNiO_{3-x}/Nb-SrTiO₃ p-n heterojunction: SCLC conduction at LRS; Schottky emission and P-F emission at HRS. c) Migration of oxygen vacancies in GdNiO_{3-x}/Nb-SrTiO₃ p-n heterojunction under electric field. V_O denotes oxygen vacancy. d) Dependence of $P(O_2)$ on the band structural of GdNiO_{3-x} films. Energy levels and work functions of the various components in the devices. The dashed dotted lines denote the Fermi level (E_F). When we apply the forward bias on sample D4, the electrons and holes movement direction is noted by the black and red arrow, respectively.

the potential barrier recovers and the device returns to HRS (LCS) (Figure 2a). The small-signal current of LRS decays with time following a power law ($I \sim t^{-\beta}$) (Figure 2e; Figure S7, Supporting Information), consistent with oxygen vacancy diffusion model.^[29,38]

To further verify that migration of oxygen vacancies indeed occurs in our devices, we performed TEM measurements and electron energy loss spectroscopy (EELS) analysis for both LRS and HRS of sample D4 (Figure 4). Compared with the as-grown state (Figure 1d), the HAADF image of LRS (Figure 4a) shows perfect crystallinity with less defects (i.e., oxygen vacancies) in the GdNiO_{3-x} layer. Conversely, the HAADF image of HRS (Figure 4b) shows much worse crystallinity with more defects in the GdNiO_{3-x} layer. More evidence comes from EELS measurements, which reveal the valence state of Ni. The measurements were performed along the direction indicated by the arrows, and spectra were recorded every ≈ 5 Å (Figure 4c for LRS and Figure 4d for HRS). For both the LRS and HRS samples, there were essentially no changes in either O K-edge or Ni L-edge EELS along the scanning pathway. However, compared with LRS, the main peak (marked by the red arrow) in HRS O K-edge EELS shifts a little to the right, implying lower Ni valence in HRS. The small pre-peak in the O K-edge (labeled by a blue arrow in Figure 4e) almost disappears in HRS, suggesting the

existence of large amount of oxygen vacancies.^[11,39] Moreover, the area ratio between L₃ and L₂ peaks in the Ni L-edge provides an estimation of Ni valence state.^[40] Higher valence of cation gives rise to a smaller ratio of L₃/L₂ due to the lower occupancy of 3d-states.^[41] The EELS spectra were normalized using the Ni L-edge and the evolution of the L₃/L₂ ratio was monitored. As shown in Figure 4f, the L₃/L₂ area ratio of HRS is statistically higher than that of LRS, confirming that HRS possesses lower Ni valence, consistent with the O K-edge result. Therefore, we conclude that oxygen vacancies indeed migrate out of GdNiO_{3-x} films in LRS and re-enter GdNiO_{3-x} films in HRS, consistent with the model proposed in Figure 3c. Further in-suit TEM measurements can be investigated by directly imaging of atomic-scale dynamic processes and their real-time impact on resistance change,^[42-44] which can give us an in-depth understanding of oxygen vacancy driven RS behavior observed here.

We have investigated the bipolar RS behavior of Pt/GdNiO_{3-x}/Nb-SrTiO₃ heterostructures, and confirmed that modification of the barrier at the GdNiO_{3-x}/Nb-SrTiO₃ interface by the migration of oxygen vacancies is the origin. Moreover, we also demonstrate that oxygen vacancies cannot be seen merely as electron donors which shift the E_F of nickelates rigidly, but strongly modify the electronic structure due to the strong electron-lattice and electron-lattice interactions in nickelates. It

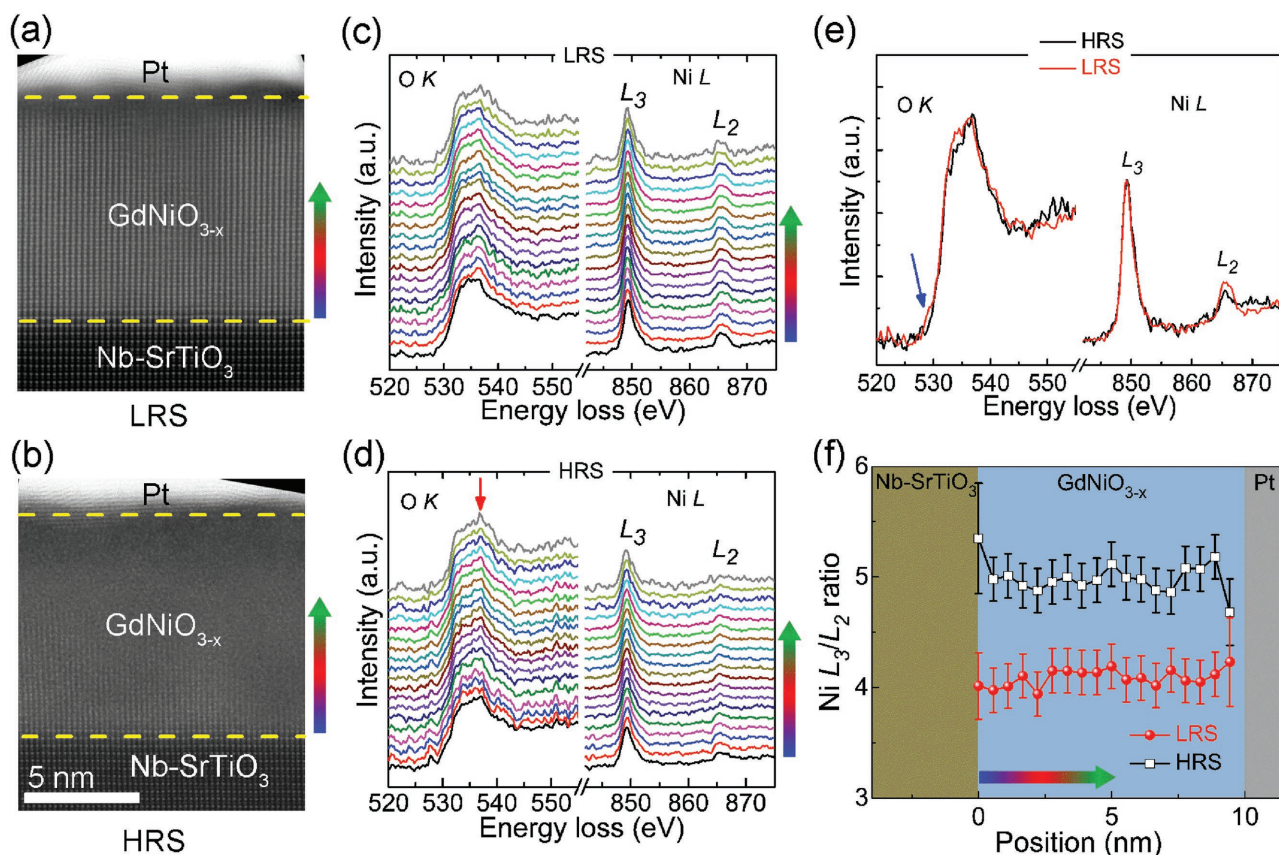


Figure 4. EELS analysis. HAADF images of a) LRS and b) HRS of sample D4. O K-edge and Ni L-edge EELS spectra along the scanning direction shown in panels (a) and (b) for c) LRS and d) HRS. e) Comparison of representative O K-edge and Ni L-edge EELS spectra for HRS and LRS. The pre-peak of O K-edge is labeled by a blue arrow. f) Comparison of Ni $L_{3/2}$ area ratio for HRS and LRS after the Ni L-edge normalization. The error bars are based on the multiple peak area calculations and the line is to assist visualization. The color arrows in the figure represent the scanning direction.

can be seen that E_F shifts toward E_V with increasing the oxygen vacancies concentration, and the nominal valence of Ni^{3+} tends to be Ni^{2+} with half filled e_g bands, enlarging the Mott–Hubbard splitting and shifting the E_C higher (see Figure 3d). More oxygen vacancies in $GdNiO_{3-x}$ films induce larger barrier (see Figure 3d) at the $GdNiO_{3-x}/Nb-SrTiO_3$ interface, thus, the HRS resistance increases with decreasing $P(O_2)$ (see Figure 1b; Figure S3, Supporting Information). Under electric field, a large modulation of the interfacial barrier can be induced by the migration of oxygen vacancies, leading to the significant resistance change of the device prepared under lower $P(O_2)$.

Note that the RS behavior is not limited to $GdNiO_{3-x}$ only, we have also investigated $Pt/RNiO_{3-x}/Nb-SrTiO_3$ heterostructures where R varies from Sm, to Gd, Er, and Lu. Generally, the tolerance factor and the Ni–O–Ni superexchange angle decrease when the size of rare earth element decreases from Sm to Lu (Figure 5a).^[8] Reducing the Ni–O–Ni superexchange angle leads to a reduction of the bandwidth, hence an increase of the U/B (where B is initial width of the Ni 3d band), which drives the system deeper into the insulating state (larger E_g or higher metal–insulator transition temperature T_{MI}).^[8] Therefore, the barrier at the $RNiO_{3-x}/Nb-SrTiO_3$ interface could show larger difference when R changes, even if $P(O_2)$ stays the same. Figure 5b shows the $I-V$ characteristics of

$Pt/RNiO_{3-x}/Nb-SrTiO_3$ devices with R changing from Sm, Gd, Er, to Lu. Indeed, more pronounced $I-V$ hysteresis characteristics and larger ON/OFF ratios are observed when we change R from Sm to Lu (Figure 5b,c). The pseudocubic lattice constants for bulk $SmNiO_3$, $GdNiO_3$, $ErNiO_3$, and $LuNiO_3$ are 3.784, 3.756, 3.70, and 3.67 Å, respectively.^[45,46] Noted that the cubic lattice constant of $SrTiO_3$ is 3.905 Å. Therefore, larger lattice mismatch will exist when we change R from Sm to Lu. The oxygen vacancies are more likely to exist in the $LuNiO_3$ (also $ErNiO_3$) films even we deposited under high oxygen pressure. That may be the reason why the ON/OFF ratio in the $LuNiO_3$ (also $ErNiO_3$) sample decreases much slower than that of $GdNiO_3$ sample with the oxygen pressure (shown in Figure 5c). Moreover, the Ni–O–Ni bond angle could be affected by the loss of oxygen ions due to the Ni–O octahedral rotation. Further experimental and theoretical investigations are needed to address whether the change of Ni–O–Ni bond angle contributes to the observed resistive switching effect.

In summary, electrochemically driven nonvolatile bipolar RS behavior is demonstrated in nickelates-based heterostructures at room temperature. A clear correlation between the RS effect and oxygen vacancies in the nickelates films is established. Large ON/OFF ratio, good retention, and fatigue performance observed in these heterostructures suggest potential application

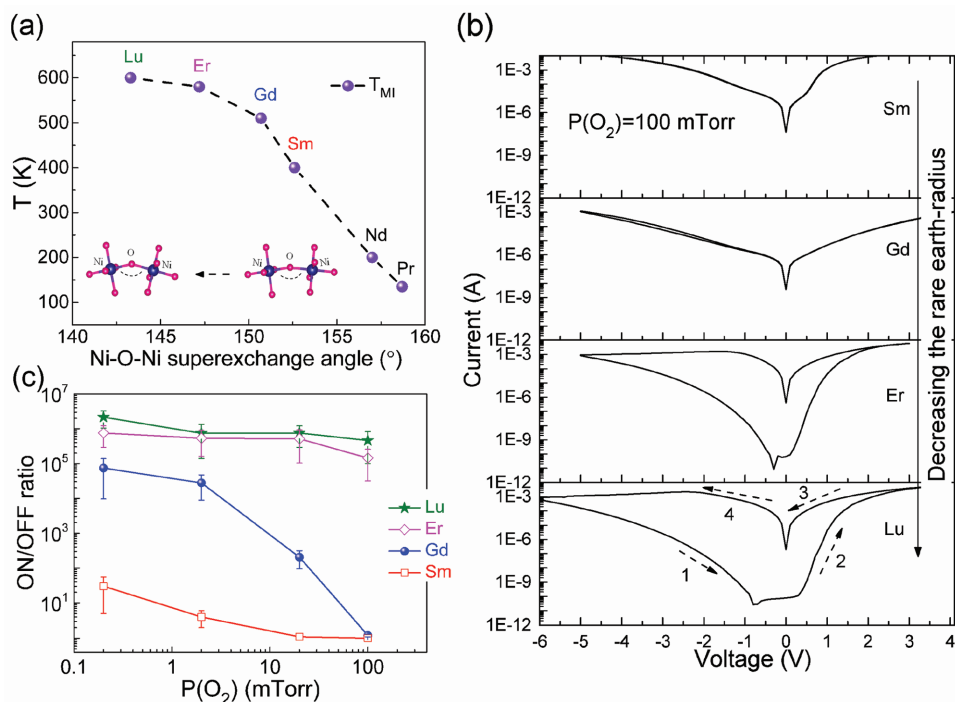


Figure 5. Comparison of ON/OFF ratio of different devices. a) The variation of the metal–insulator transition temperature T_{MI} as a function of the Ni–O–Ni superexchange angle in the $RNiO_3$ series. The inset shows the schematic of the decrease of the Ni–O–Ni superexchange angle from Sm (152.6°) to Lu (143.3°).^[8] b) I – V characteristics for the Pt/ $RNiO_{3-x}$ /Nb–SrTiO₃ devices with R changing from Sm, Gd, Er, to Lu. All $RNiO_{3-x}$ films were deposited under 100 mTorr. c) Dependence of the ON/OFF ratio on $P(O_2)$ for Pt/ $RNiO_{3-x}$ /Nb–SrTiO₃ heterostructures with R changing from Sm to Lu.

in nonvolatile resistive memory. Moreover, the voltage-controlled continuous change in resistance could also be used in multilevel computing and neuromorphic devices. Overall, our finding provides an important step toward the development of multifunctional electronic devices based on nickelates.

Experimental Section

Sample Preparation: $RNiO_{3-x}$ thin films were grown on the (001)-oriented SrTiO₃ (STO), and 0.7 wt% Nb-doped SrTiO₃ (Nb-STO) substrates by pulsed laser deposition. The laser pulse (248 nm) energy density was ≈ 2 J cm⁻² and the repetition rate is 5 Hz. The substrates were heated to 725 °C during deposition. The thickness of $RNiO_{3-x}$ films was controlled to be about 10 nm. After deposition, the samples were in situ annealed for 10 min, then cooled down to room temperature. The surface morphology of the $RNiO_{3-x}$ films was examined using atomic force microscope.

Structure Characterization: X-ray diffraction measurement was conducted to identify the crystal structure by using Rigaku SmartLab instrument. The high-angle annular-dark-field images of the films were obtained using an ARM-200F (JEOL, Tokyo, Japan) STEM operated at 200 kV with a CEOS Cs corrector (CEOS GmbH, Heidelberg, Germany) to cope with the probe-forming objective spherical aberration. HAADF images were acquired at acceptance angles of 90–250 mrad. The attainable resolution in HAADF images is better than 0.078 nm.

Electrical Characterizations: For the electrical measurements, square Pt top electrodes of 70 $\mu\text{m} \times 70 \mu\text{m}$ and a thickness of 30 nm were deposited on the $RNiO_{3-x}$ films using a metal shadow mask. The electrical properties of the Pt/ $RNiO_{3-x}$ /Nb–SrTiO₃ heterostructures were measured using a pA metre/direct current (DC) voltage source (Hewlett Package 4140B) on a low noise probe station under air

condition at room temperature. A compliance current of 10 mA was applied to the set operation to prevent the device from permanent breakdown. Agilent 4294 A was used to measure the capacitance–voltage in a frequency range from 1 kHz to 1 MHz with a fixed oscillating voltage of 10 mV. Bias voltages were applied on the Pt top electrodes with Nb–SrTiO₃ grounded. Voltage pulses were supplied by an arbitrary waveform generator (Agilent 33522A). For the fatigue measurements, the voltage stresses were applied using a Multiferroic tester (Radiant Technologies).

Supporting Information

Supporting Information is available from the Wiley Online Library or from the author.

Acknowledgements

L.W. and Q.Z. contributed equally to this work. K.J. and L.G. acknowledge support from the National Basic Research Program of China (Grant Nos. 2014CB921001 and 2014CB921002), the National Natural Science Foundation of China (Grant Nos. 11134012, 51522212, 51421002, and 11574365), and the Strategic Priority Research Program of Chinese Academy of Sciences (Grant No. XDB07030200). The authors acknowledge financial support from the Ministry of Education, Singapore under the Grant Nos. MOE2013-T2-1-052 and MOE2014-T2-1-099.

Conflict of Interest

The authors declare no conflict of interest.

Keywords

heterostructures, memory, nickelates, oxygen vacancy, resistive switching

Received: July 19, 2017
Published online:

- [1] J. Liu, M. Kargarian, M. Kareev, B. Gray, P. J. Ryan, A. Cruz, N. Tahir, Y.-D. Chuang, J. Guo, J. M. Rondinelli, J. W. Freeland, G. A. Fiete, J. Chakhalian, *Nat. Commun.* **2013**, *4*, 2714.
- [2] J. Shi, S. D. Ha, Y. Zhou, F. Schoofs, S. Ramanathan, *Nat. Commun.* **2013**, *4*, 2676.
- [3] R. Jaramillo, S. D. Ha, D. Silevitch, S. Ramanathan, *Nat. Phys.* **2014**, *10*, 304.
- [4] M. Först, A. D. Caviglia, R. Scherwitzl, R. Mankowsky, P. Zubko, V. Khanna, H. Bromberger, S. B. Wilkins, Y.-D. Chuang, W. S. Lee, W. F. Schlotter, J. J. Turner, G. L. Dakovski, M. P. Minitti, J. Robinson, S. R. Clark, D. Jaksch, J.-M. Triscone, J. P. Hill, S. S. Dhesi, A. Cavalleri, *Nat. Mater.* **2015**, *14*, 883.
- [5] T. H. Kim, D. Puggioni, Y. Yuan, L. Xie, H. Zhou, N. Campbell, P. J. Ryan, Y. Choi, J.-W. Kim, J. R. Patzner, S. Ryu, J. P. Podkaminer, J. Irwin, Y. Ma, C. J. Fennie, M. S. Rzchowski, X. Q. Pan, V. Gopalan, J. M. Rondinelli, C. B. Eom, *Nature* **2016**, *533*, 68.
- [6] Y. Zhou, X. Guan, H. Zhou, K. Ramadoss, S. Adam, H. Liu, S. Lee, J. Shi, M. Tsuchiya, D. D. Fong, S. Ramanathan, *Nature* **2016**, *534*, 231.
- [7] L. Wang, S. Ju, L. You, Y. Qi, Y. Guo, P. Ren, Y. Zhou, J. Wang, *Sci. Rep.* **2015**, *5*, 18707.
- [8] G. Catalan, *Phase Transitions* **2008**, *81*, 729.
- [9] M. T. Curnan, J. R. Kitchin, *J. Phys. Chem. C* **2014**, *118*, 28776.
- [10] L. Wang, S. Dash, L. Chang, L. You, Y. Feng, X. He, K. Jin, Y. Zhou, H. G. Ong, P. Ren, S. Wang, L. Chen, J. Wang, *ACS Appl. Mater. Interfaces* **2016**, *8*, 9769.
- [11] L. Wang, L. Chang, X. Yin, L. You, J. Zhao, H. Guo, K. Jin, K. Ibrahim, J. Wang, A. Rusydi, J. Wang, *Appl. Phys. Lett.* **2017**, *110*, 043504.
- [12] S. Wu, H. Peng, T. Wu, *Appl. Phys. Lett.* **2011**, *98*, 093503.
- [13] Z. T. Xu, K. J. Jin, L. Gu, Y. L. Jin, C. Ge, C. Wang, H. Z. Guo, H. B. Lu, R. Q. Zhao, G. Z. Yang, *Small* **2012**, *8*, 1279.
- [14] Z. Yan, J.-M. Liu, *Sci. Rep.* **2013**, *3*, 2482.
- [15] P. Sharma, S. Ryu, J. D. Burton, T. R. Paudel, C. W. Bark, Z. Huang, Ariando, E. Y. Tsymbal, G. Catalan, C. B. Eom, A. Gruverman, *Nano Lett.* **2015**, *15*, 3547.
- [16] C. Wang, K.-J. Jin, Z.-T. Xu, L. Wang, C. Ge, H.-B. Lu, H.-Z. Guo, M. He, G.-Z. Yang, *Appl. Phys. Lett.* **2011**, *98*, 192901.
- [17] L. Wang, K. Jin, C. Ge, C. Wang, H. Guo, H. Lu, G. Yang, *Appl. Phys. Lett.* **2013**, *102*, 252907.
- [18] L. Wang, Z. Wang, K.-j. Jin, J. Li, H. Yang, C. Wang, R. Zhao, H. Lu, H. Guo, G. Yang, *Appl. Phys. Lett.* **2013**, *102*, 242902.
- [19] S. Choopun, R. Vispute, W. Noch, A. Balsamo, R. Sharma, T. Venkatesan, A. Iliadis, D. C. Look, *Appl. Phys. Lett.* **1999**, *75*, 3947.
- [20] Z. Zhang, P. Wu, L. Chen, J. Wang, *Appl. Phys. Lett.* **2010**, *96*, 232906.
- [21] S. Wu, X. Luo, S. Turner, H. Peng, W. Lin, J. Ding, A. David, B. Wang, G. Van Tendeloo, J. Wang, T. Wu, *Phys. Rev. X* **2013**, *3*, 041027.
- [22] Z. Sun, Y. Zhao, M. He, L. Gu, C. Ma, K. Jin, D. Zhao, N. Luo, Q. Zhang, N. Wang, W. Duan, C.-W. Nan, *ACS Appl. Mater. Interfaces* **2016**, *8*, 11583.
- [23] A. Baikalov, Y. Q. Wang, B. Shen, B. Lorenz, S. Tsui, Y. Y. Sun, Y. Y. Xue, *Appl. Phys. Lett.* **2003**, *83*, 957.
- [24] R. Waser, R. Dittmann, G. Staikov, K. Szot, *Adv. Mater.* **2009**, *21*, 2632.
- [25] V. Vashook, S. Tolochko, I. Yushkevich, L. Makhnach, I. Kononyuk, H. Altenburg, J. Hauck, H. Ullmann, *Solid State Ionics* **1998**, *110*, 245.
- [26] R. Scherwitzl, P. Zubko, I. G. Lezama, S. Ono, A. F. Morpurgo, G. Catalan, J. M. Triscone, *Adv. Mater.* **2010**, *22*, 5517.
- [27] L. Wang, Y. Jin, K. Jin, C. Wang, H. Lu, C. Wang, C. Ge, X. Chen, E. Guo, G. Yang, *Europhys. Lett.* **2011**, *96*, 17008.
- [28] J. Park, D.-H. Kwon, H. Park, C. U. Jung, M. Kim, *Appl. Phys. Lett.* **2014**, *105*, 183103.
- [29] E. Mikheev, B. D. Hoskins, D. B. Strukov, S. Stemmer, *Nat. Commun.* **2014**, *5*, 3990.
- [30] J. J. Yang, I. H. Inoue, T. Mikolajick, C. S. Hwang, *MRS Bull.* **2012**, *37*, 131.
- [31] H. Y. Peng, G. P. Li, J. Y. Ye, Z. P. Wei, Z. Zhang, D. D. Wang, G. Z. Xing, T. Wu, *Appl. Phys. Lett.* **2010**, *96*, 192113.
- [32] K. Zheng, J. L. Zhao, X. W. Sun, V. Q. Vinh, K. S. Leck, R. Zhao, Y. G. Yeo, L. T. Law, K. L. Teo, *Appl. Phys. Lett.* **2012**, *101*, 143110.
- [33] M. A. Lampert, *Phys. Rev.* **1956**, *103*, 1648.
- [34] K. C. Kao, *Dielectric Phenomena in Solids*, Elsevier Academic, San Diego, CA **2004**.
- [35] J. Yeargan, H. Taylor, *J. Appl. Phys.* **1968**, *39*, 5600.
- [36] T. Harada, I. Ohkubo, K. Tsubouchi, H. Kumigashira, T. Ohnishi, M. Lippmaa, Y. Matsumoto, H. Koinuma, M. Oshima, *Appl. Phys. Lett.* **2008**, *92*, 222113.
- [37] J. S. Choi, J.-S. Kim, I. R. Hwang, S. H. Hong, S. H. Jeon, S.-O. Kang, B. H. Park, D. C. Kim, M. J. Lee, S. Seo, *Appl. Phys. Lett.* **2009**, *95*, 022109.
- [38] A. A. Bessonov, M. N. Kirikova, D. I. Petukhov, M. Allen, T. Ryhänen, M. J. Bailey, *Nat. Mater.* **2015**, *14*, 199.
- [39] J. Gazquez, W. Luo, M. P. Oxley, M. Prange, M. A. Torija, M. Sharma, C. Leighton, S. T. Pantelides, S. J. Pennycook, M. Varela, *Nano Lett.* **2011**, *11*, 973.
- [40] S. Muto, Y. Sasano, K. Tatsumi, T. Sasaki, K. Horibuchi, Y. Takeuchi, Y. Ukyo, *J. Electrochem. Soc.* **2009**, *156*, A371.
- [41] Z. Wang, J. Yin, Y. Jia, *Micron* **2000**, *31*, 571.
- [42] P. Gao, Z. Wang, W. Fu, Z. Liao, K. Liu, W. Wang, X. Bai, *Micron* **2010**, *41*, 301.
- [43] K. Baek, S. Park, J. Park, Y.-M. Kim, H. Hwang, S. H. Oh, *Nanoscale* **2017**, *9*, 582.
- [44] L. Yao, S. Inkinen, S. van Dijken, *Nat. Commun.* **2017**, *8*, 14544.
- [45] J. Rodríguez-Carvajal, S. Rosenkranz, M. Medarde, P. Lacorre, M. T. Fernández-Díaz, F. Fauth, V. Trounov, *Phys. Rev. B* **1998**, *57*, 456.
- [46] J. A. Alonso, M. J. Martínez-Lope, M. T. Casais, J. L. García-Muñoz, M. T. Fernández-Díaz, *Phys. Rev. B* **2000**, *61*, 1756.